Quaternary Sediment Thicknesses, Paleochannels, and Hazard Assessment Revealed by a 6200-Station Array in the Guangdong–Hong Kong–Macao Greater Bay Area, South China

Cheng Xiong[1,2,3], Yangfan Deng[*1], Xiuwei Ye[2], Liwei Wang[2], Yanxin Zhang[2], Zuoyong Lv[2], Xiaona Wang[2], Xuan Gong[2], and Xiaobo He[4]

ABSTRACT

The Guangdong–Hong Kong–Macao Greater Bay area, a highly populated region, plays a vital role in the economic development of East Asia. Its construction and development rely on accurately characterizing near-surface loose sediment layers. However, traditional drilling and active source methods are often impractical for large-scale exploration in densely populated areas due to their high costs and destructive nature. To overcome this shortage, a dense array comprising 6214 stations was deployed and the noise horizontal-to-vertical spectral ratio method was employed to determine the fundamental frequency (f_0) and peak amplitude. The Quaternary sediment thickness was further estimated based on their empirical relationships with f_0. More importantly, several buried paleochannels were identified, manifesting deep valleys on the vertical section and curved stripes on the horizontal section. Combining regional drilling data and sites of geological hazards in the past, we conclude that the paleochannels are zones of high seismic and geological hazard. This study provides a scientific basis for urban construction and disaster prevention.

KEY POINTS

- A 6214 station array and horizontal-to-vertical spectral ratio (HVSR) method were used to explore the surface structure of a densely populated area.
- The Quaternary sediment thickness was estimated and buried paleochannels were characterized in detail.
- Geological and geophysical analyses highlight that paleochannels are zones of high geological hazard.

Supplemental Material

INTRODUCTION

Guangdong–Hong Kong–Macao Greater Bay area (GBA) in coastal South China, covered by thick sediments, is the most populous built-up metropolitan area globally, which plays a vital role in the economic development in East Asia. Loose, unconsolidated sediments can significantly amplify seismic ground motion, damaging buildings, structures, and infrastructure (Seed *et al.*, 1988; Guéguen *et al.*, 1998; Panou *et al.*, 2005). Hence, accurate characterization of near-surface sediments is crucial in predicting ground motion and mitigating these seismic and geologic disasters, particularly in densely developed urban areas (Olsen, 2000). In addition, numerous buried paleochannels composed of soft, thick sediments pose risks to urban engineering construction (Sairam *et al.*, 2018). Therefore, a comprehensive survey of near-surface sediments in the GBA is urgently needed to provide high-resolution seismic parameters for urban construction and disaster prevention.

1. State Key Laboratory of Deep Earth Processes and Resources, Guangzhou Institute of Geochemistry, Chinese Academy of Sciences, Guangzhou, China, https://orcid.org/0000-0003-3994-9865 (YD); 2. CEA Key Laboratory of Earthquake Monitoring and Disaster Mitigation Technology, Guangdong Earthquake Agency, Guangzhou, China, https://orcid.org/0000-0002-7648-3307 (YZ); 3. College of Earth and Planetary Sciences, University of Chinese Academy of Sciences, Beijing, China; 4. Marine Science and Technology College, Zhejiang Ocean University, Zhoushan, Zhejiang, China, https://orcid.org/0000-0002-6357-8948 (XH)

*Corresponding author: yangfandeng@gig.ac.cn

Cite this article as Xiong, C., Y. Deng, X. Ye, L. Wang, Y. Zhang, Z. Lv, X. Wang, X. Gong, and X. He (2025). Quaternary Sediment Thicknesses, Paleochannels, and Hazard Assessment Revealed by a 6200-Station Array in the Guangdong–Hong Kong–Macao Greater Bay Area, South China, *Bull. Seismol. Soc. Am.* **XX**, 1–13, doi: 10.1785/0120240214

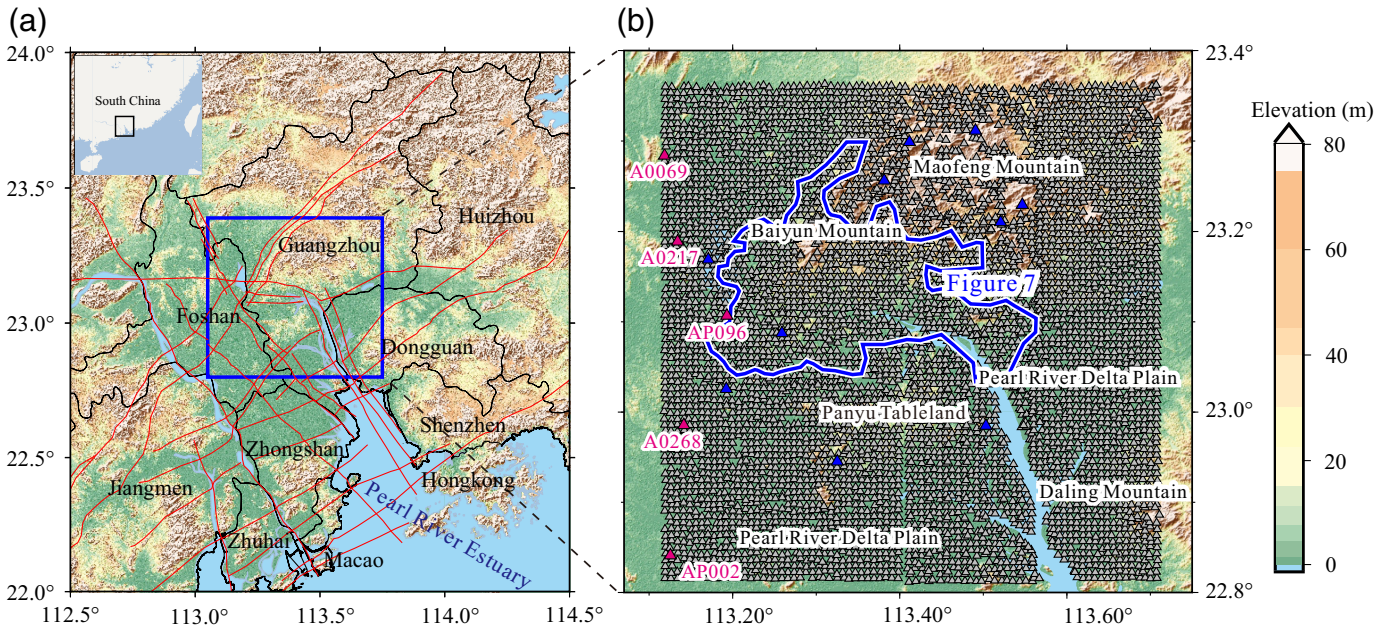

Figure 1. Topography of the study area and distribution of seismic stations. (a) Topography of the study area. The blue box outlines the region for stations. The distribution faults represented by solid red lines, are based on data from the Guangdong Geological Survey Institute. Main cities are marked with black words. The thin black lines represent the city boundaries. (b) Distribution of seismic stations. The red triangles indicate the seismic stations used in Figures 2 and 4. The blue triangles indicate the reference seismic stations used in the standard spectral ratio analyses. The blue line outlines the region for the borehole data. The color version of this figure is available only in the electronic edition.

Previous near-surface sediment investigations in the GBA have primarily relied on geological boreholes and active source surveys (Zhuang *et al.*, 2015). However, using active sources such as explosives and some mechanical sources can damage the surrounding environment and disturb residents. Similarly, drilling methods are environmentally harmful and expensive. Therefore, both active source and drilling techniques are unsuitable for large-scale investigations in urban areas. In recent decades, using ambient noise seismic data to investigate shallow and deep crust structures has been confirmed as an innovative approach. Xiong *et al.* (2024) utilized ambient noise tomography to develop a 0–5 km *S*-wave velocity model. However, the resolution of this model is limited to depths shallower than 400 m. The horizontal-to-vertical spectral ratio (HVSR) method is a technique that utilizes ambient seismic noise data to investigate near-surface structures. It was first proposed by Nogoshi and Igarashi (1971), building on the initial microtremor studies of Kanai and Tanaka (1961). Nakamura (1989) further developed this method, suggesting that HVSR can be used to estimate the resonance frequency and seismic amplification factor of sites covered with soft soil layers. Because of its simplicity, cost-effectiveness, and environmental friendliness, the HVSR method has shown promise in estimating sediment thickness and providing a direct assessment of local site effects (Molnar *et al.*, 2022). However, the amplitude of the HVSR is not directly linked to actual amplification (Perron *et al.*, 2018), which means that additional methods are needed to estimate site amplification effects. One widely used approach for studying site effects is the standard spectral ratio (SSR) method (Borcherdt, 1970). This method calculates the ratio of the Fourier spectra of seismic ground motion between the target station and reference bedrock sites. The SSR method has been widely used for analyzing site response (Pratt and Schleicher, 2021; Song and Yang, 2022; Zhou and Yao, 2024). By combining the results of HVSR and SSR, we can better understand the relationship between sedimentary structure and amplification effects.

In this study, we deployed a 6214 station dense array located in the central GBA (Fig. 1), covering the metropolitan area of Guangzhou city and parts of Foshan and Dongguan. The spacing and dimension of the array are notably comparable with that in Long Beach, California (Lin *et al.*, 2013). Based on the HVSR method, we determined the distribution of the fundamental frequency (f_0) and the peak amplitude (A_0) across the study area. We also established a relationship between f_0 and Quaternary sediment thickness, revealing the distribution of sediments and paleochannel characteristics. Finally, we assessed the potential impact of paleochannel areas on seismic and geological hazards. These findings have significant implications for evaluating ground stability and possible dangers and providing valuable insights for urban construction and disaster mitigation in urban areas.

DATA AND METHOD

Data

To provide valuable information for urban construction and disaster risk assessment in the most populated area in the world, we deployed a dense seismic array, named GBArray-I, comprising

6214 three-component seismic nodes within the urban area, including Guangzhou city and part of Dongguan city and Foshan city, from December 2020 to January 2021 (Fig. 1). This temporary array consisted of a static network and a mobile network. The static network included 707 seismic stations spaced 2.25 km apart, which were recorded continuously for 30–35 days. The mobile network comprised 5507 mobile seismic stations spaced 0.75 km apart, which recorded data continuously for 3–20 days. The study region covers ~60 km × 60 km, with a station spacing of about 750 m. Three types of seismic nodes, namely EPS (with a corner frequency of 5 s), SmartSolo (with a corner frequency of 5 Hz), and Zland-3C (with a corner frequency of 5 Hz), were involved in the observation. These types of nodal seismometers all exhibit good performance below their corner frequencies (Zhou and Shen, 2021; Dong *et al.*, 2022; Zeckra *et al.*, 2022). The sampling frequency of waveforms was 250 Hz. To alleviate the influence of wind-generated perturbations, all seismometers were directly buried on the ground surface. For more information on the deployment and instrument details, please refer to Ye *et al.* (2024). In addition, the 3576 boreholes collected in the central part of the study area (outlined by the blue line in Fig. 1b) provide benchmarks for the thickness of the Quaternary sedimentary layers.

From the National Earthquake Data Center, we selected five regional and teleseismic earthquakes with high signal-to-noise ratios (SNRs) for SSR analysis. The SNR is defined as the ratio of the maximum amplitude of the *S*-wave signal envelope to the average amplitude of the noise envelope that precedes the *P* wave. For each event, we retained only those stations where the SNR for both east–west and north–south components was greater than three for further analysis. Because of the low seismic activity in the region, only one local earthquake (with an epicentral distance of less than 300 km) was selected for the analysis. The detailed information about all the events analyzed in this study is listed in Table S1, available in the supplemental material to this article.

METHOD

HVSR analysis

The noise-based HVSR method analyzes three-component microtremor recordings, enabling the rapid and straightforward determination of sediment fundamental frequency (Lachet and Bard, 1994; Site Effects Assessment Using Ambient Excitations [SESAME], 2004). HVSR curves are computed as the ratio of the Fourier amplitude spectra (FAS) of the horizontal and vertical components from the microtremor record (Picozzi *et al.*, 2005). On 1D site configurations, the peak frequency derived from the HVSR method is widely acknowledged as a reliable estimate of the fundamental frequency of a soil layer (Pontrelli *et al.*, 2023). Because of its advantages, the method has been applied to various complex site conditions, including thermal-basin (Agostini *et al.*, 2015), glaciers (Picotti *et al.*, 2017), Antarctica (Yan *et al.*, 2018), seafloor (Farazi *et al.*, 2023), and urban areas (Chen *et al.*, 2009; Gallipoli *et al.*, 2020; Maklad *et al.*, 2020). The HVSR method is particularly effective in detecting shallow interfaces due to its high sensitivity to strong impedance contrasts. It excels at identifying the boundaries between near-surface soft and hard soil layers, a task that traditional ambient noise tomography often struggles to accomplish.

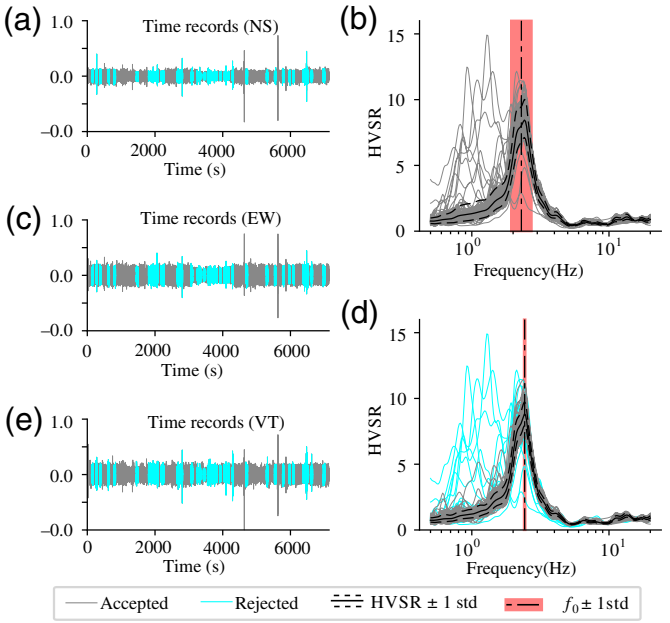

Figure 2. An example of ambient noise record processed using hvsrpy. (a,c,e) Three-component microtremor records at station A0217 (see Fig. 1 for station locations). The cyan time windows represent those rejected using the frequency-domain window-rejection algorithm (FWA). (b) Horizontal-to-vertical spectral ratio (HVSR) curves were obtained before applying the FWA. (d) HVSR curves were obtained after applying the FWA, in which the cyan curves represent those rejected. The color version of this figure is available only in the electronic edition.

We obtained HVSR curves using the Python package hvsrpy version 1.0.0 (Vantassel, 2021), in which the noise processing procedure followed the scheme designed by Cox *et al.* (2020). The FAS of the horizontal components are obtained by the geometric mean of the east–west, north–south components. Traditional methods often apply the average amplitude ratio algorithm of short-time to long-time windows to remove transient interference signals, enhancing accuracy in measuring HVSR curves (Wathelet *et al.*, 2020). In contrast, the hvsrpy applies an automatic frequency-domain window-rejection algorithm (FWA) to remove contaminated time windows. Figure 2 exemplifies the utilization of hvsrpy for processing the noise data of station A0217. After applying the FWA with $n = 2$ (n is the number of standard deviations from the median f_0-value), the peak frequency shifts from 2.32 to 2.40 Hz, whereas the standard deviation decreases from 0.17 to 0.01.

For each station, a selected 2 hr data segment was partitioned into 60 s time windows, and the HVSR curve was calculated for each window. We used the Konno–Ohmachi

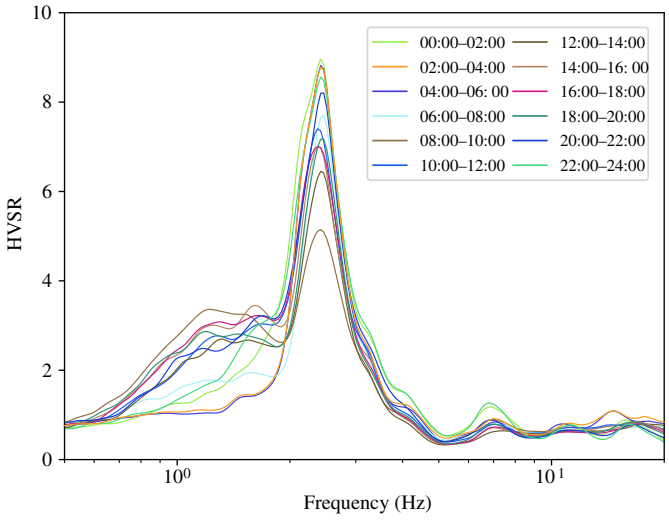

Figure 3. HVSR curves at station A0217 at different periods with a 2 hr time window on 19 January 2021. The color version of this figure is available only in the electronic edition.

smoothing algorithm with a bandwidth coefficient (b) of 40 to strengthen the stability of the HVSR curves (Konno and Ohmachi, 1998). HVSR was resampled logarithmically between 0.5 and 20 Hz using 200 points. To select an appropriate time window for calculating HVSR, we conducted a detailed comparison among different hours of the day (Fig. 3). It can be observed that the fundamental frequencies of the HVSR curves remain relatively consistent across various periods, whereas the amplitudes show some variation. To minimize the impact of human activities, we selected 2 hr continuous data of each station between 2 and 4 a.m. to calculate the HVSR curves, following Bao *et al.* (2018).

Fundamental frequency and its associated peak amplitude determination

For each site, the peak frequency and its associated peak amplitude can be estimated from the HVSR curves. The peak frequency of the HVSR curve is always considered as the fundamental frequency (f_0) of the sedimentary layer (Lunedei and Albarello, 2010; Peng *et al.*, 2020). The different HVSR curves can be categorized into four types, following the classification of Yang *et al.* (2019). The first type exhibits a single prominent peak with an amplitude exceeding 2 (Fig. 4b), suggesting the presence of a significant seismic impedance interface between loose deposits and the underlying rock (Chatelain *et al.*, 2008). The second type displays multiple distinct peaks with comparable amplitudes (Fig. 4c), indicating the possible occurrence of multiple sharp shear-wave velocity contrasts in the subsurface (Woolery and Street, 2002; Dal Moro and Panza, 2022). Following previous research, we considered the lowest frequency peak as the f_0 of the measured sites (Beroya *et al.*, 2009; Sivaram *et al.*, 2012). The third type exhibits a broad peak (Fig. 4d), which may be attributed to the existence of an inclined interface between softer and harder layers beneath the surface (Woolery and Street, 2002; Sivaram *et al.*, 2012) or significant 2D or 3D variations of the underground structure that generate a complex wavefield (Thompson *et al.*, 2012; Pilz and Cotton, 2019). The f_0 for this type of curve was determined based on the maximum amplification, following Beroya *et al.* (2009). The fourth type appears flat, with amplitudes below 2 and without any discernible reliable peak (Fig. 4e). Hence, we did not pick an f_0-value for this category of curves.

Sediment thickness estimation

Under the condition of a strong impedance between the sediment and bedrock, the thickness of sediment can be related to the average shear-wave velocity (V_S) of the sediment and the f_0 using the quarter-wavelength approach (Peng *et al.*, 2020). When the value of V_S is hard to determine, the thickness of the sedimentary layer can be estimated with an empirical equation (Ibs-von Seht and Wohlenberg, 1999),

$$h = af_0^b, \tag{1}$$

in which h is the thickness of the sediments, a and b are fitting parameters that can be calculated through least-squares fitting when h-values are available from borehole data. In this article, we utilize equation (1) to determine the thickness of sediments due to the lack of accurate V_S-values.

SSR analysis

To minimize the impact of instrument type on the SSR analysis, we selected 496 stations from the static network that were equipped with Zland 3C short-period seismometers for the SSR analysis. A crucial step in SSR analysis is selecting reference stations, which should be located on bedrock sites. Based on the station deployment logs and HVSR results, we selected 10 stations as reference stations (indicated by the blue triangles in Fig. 1b). We then used the average spectrum of the selected 10 stations as the reference spectrum, which helps mitigate the instability of individual reference stations.

During the one-month recording period, six high SNR earthquakes were selected for further analysis, which included five regional and teleseismic events, as well as one local earthquake event (Table S1). Because the signals above 2 Hz were weak, only the relatively low-frequency range (0.1–2 Hz) was analyzed for the regional and teleseismic earthquakes (Zhou and Yao, 2024). Local earthquake usually exhibits stronger energy in the high-frequency range and was analyzed within the frequency range of 0.5–10 Hz. We focused on the horizontal-component S-wave records. The signal window was 15 s after the S-wave arrival for local earthquakes and 50 s for regional and teleseismic earthquakes. We calculated the FAS for the east–west and north–south components, then obtained the horizontal-component amplitude spectrum using geometric averaging. For each event, the spectral ratio for each station

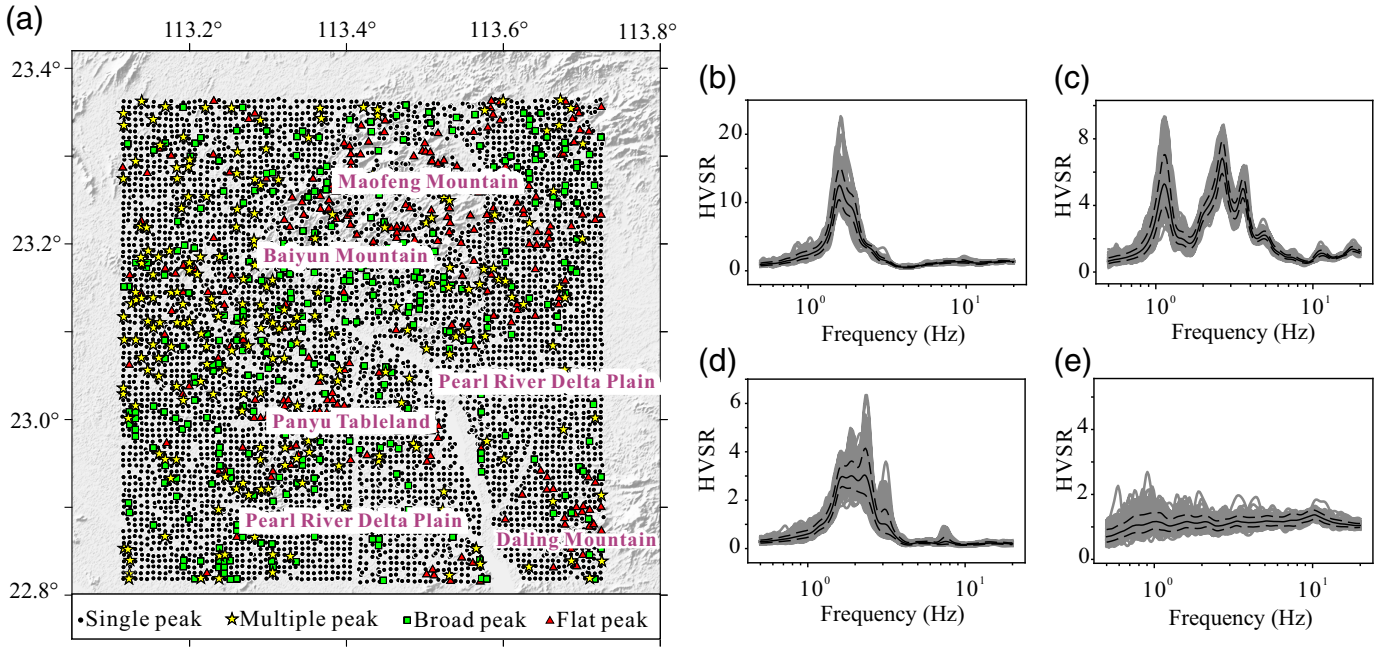

Figure 4. Classification of HVSR curves and distribution in the study area. The black circles represent single-peak HVSR curves, the yellow stars represent multiple-peak HVSR curves, the green squares represent broad-peak HVSR curves and the red triangles represent flat HVSR curves. (a) Distribution of the four types of HVSR curves. (b–e) Examples of four typical HVSR curves (see Fig. 1 for station locations). (b) Station AP002 with a single clear peak. (c) Station AP096 with three peaks. (d) Station A0268 with a broad peak. (e) Station A0069 without clear peak. The color version of this figure is available only in the electronic edition.

was calculated by dividing the horizontal spectrum by the average horizontal spectrum of 10 reference stations. At each station, the spectral ratios for *S* waves from both regional and teleseismic earthquakes were then averaged at each station within the 0.1–2 Hz frequency range.

RESULTS

HVSR curves

After excluding sites with anomalous data, we obtained HVSR curves for 6046 stations within the dense seismic array. Figure 4a displays the distribution of the four types of curves. The single-peak-type HVSR curve is the predominant category within our dataset, consisting of a total of 5168 curves, which accounts for ~85% of the whole. The multiple-peak-type sites, totaling 269, represent about 4% and are predominantly located in the western part of the study area. The broad-peak-type sites, totaling 337 (about 6%), are primarily situated along the slope or in the transition zone from the hilly part to the floodplain. The flat-type curves, which number 275 and account for about 4%, are mainly distributed in the mountain area, where bedrock is often exposed at the surface.

Fundamental frequency and peak amplitude

Upon analyzing the HVSR curves of all sites, the fundamental frequency (f_0) and the associated amplitude (A_0) are presented in Figure 5. The clear distinction between the high and low values of f_0 and A_0 closely aligns with the fault location. This correlation strongly suggests that the fault plays a significant role in shaping the near-surface structure of the area. The f_0-values range mainly from 0.7 to 8.0 Hz, and its spatial distribution correlates well with the topography and surface geology of the study area. The northern, central, and southeastern regions, characterized by mountainous terrain, exhibit f_0-values exceeding 4.5 Hz, indicating a thinner coverage of loose sediment. In contrast, the southern part of the study area, which encompasses the Pearl River Delta (PRD) Plain, displays f_0-values below 3 Hz, suggesting the presence of a thicker layer with loose sediment. The f_0-values of 0.5–1.5 Hz are concentrated in the PRD Plain, forming several distinct curved stripes, indicating the presence of banded, relatively thicker sediment layers. Most A_0-values fall within the range of 3–12, exhibiting a negative correlation with f_0. Although A_0 aligns with the surface geology of the study area, it is generally acknowledged that the peak amplitude of HVSR underestimates site amplification (SESAME, 2004). Hence, we did not consider this parameter a primary indicator in further discussions.

Thickness of Quaternary sediment

Based on equation (1), we fitted the relationship between the thickness of sediments and the f_0 using the 3576 boreholes collected in the central area of our study area. The boreholes within a 50 m radius of each HVSR measurement site were matched with the f_0 site. The closest borehole was selected for the match when multiple boreholes were available. Consequently, 104 f_0 measurements and their corresponding boreholes were successfully matched, as shown in Figure 6a. By

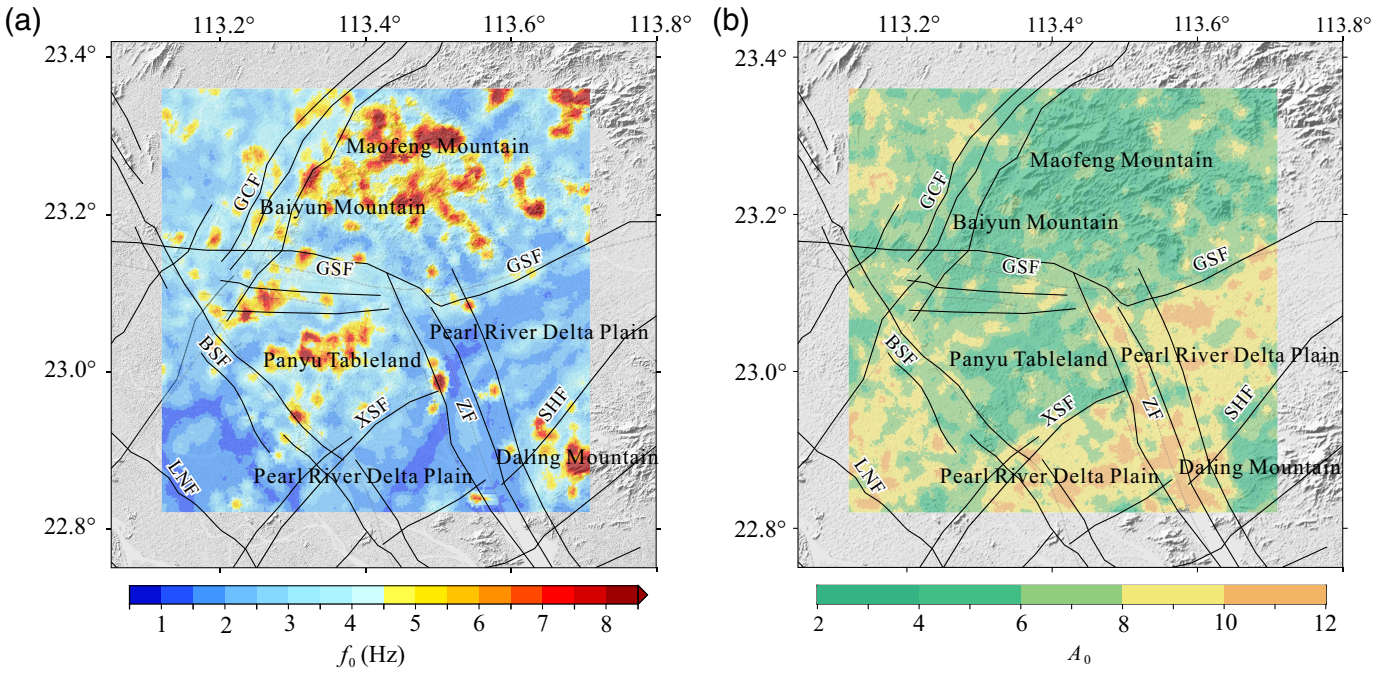

Figure 5. Distribution of (a) fundamental frequencies and (b) peak amplitude across the study area. The black solid lines mark the faults. BSF, Baini–Shawan fault; GCF, Guangzhou–Conghua fault; GSF, Guangzhou–Sanshui fault; LNF, Leliu–Nanlang fault; SHF, Shilong–Houjie fault; XSF, Xinhui–Shiqiao fault; ZF, Zhujiangkou fault. The color version of this figure is available only in the electronic edition.

fitting the Quaternary sediment thickness of matched boreholes and the f_0 measurements, we derived equation (2) to estimate the Quaternary sediment thickness in the study area:

$$h = 48.87 f_0^{(-0.95)}. \quad (2)$$

The coefficient of determination (R^2) is 0.78. Equation (2) we obtained is close to the equation determined by Liang *et al.* (2018) (blue line in Fig. 6a), who also utilized boreholes and HVSR measurements in the PRD.

The thickness of the Quaternary loose layer was determined at all measuring stations (Fig. 6b). Figure 6c,d displays histograms of the f_0-values and the Quaternary sediment thickness. The thickness of the Quaternary sedimentary layer corresponds well with the topography and surface geology of the area, with the majority of regions falling within the range of 10–30 m. In the central, northern, and southeastern parts of the study area, which are mountainous, the thickness of the Quaternary sedimentary layer ranges from 0 to 10 m. Conversely, the southern, known as the PRD Plain, exhibits Quaternary sedimentary layer thickness ranging from 20 to 45 m. The precise boundary observed between the high and low values of Quaternary sedimentary layer thickness is notably consistent with the distribution of fault locations. This observation strongly suggests that the regional fault structure plays a significant role in controlling the thickness of the Quaternary sedimentary layer in the PRD region. In the southern region of the study area, there is a distinctive pattern of curved anomalies resembling a river. These anomalies are characterized by higher thickness levels ranging from 30 to 45 m. A detailed analysis of this phenomenon is discussed in the Identification and characteristics of the paleochannels section.

DISCUSSION

Validation of the Quaternary sediment thickness by comparison with boreholes

The empirical equation (1) was developed based on the assumption of a uniform velocity–depth function across all measured sites, as proposed by Ibs-von Seht and Wohlenberg (1999). The parameters a and b in equation (1) depend on the specific relationship between shear-wave velocity and sediment depth, which varies across different regions and is primarily influenced by sedimentary composition and compaction variations. When the sediment is soft, it causes a decrease in the average shear-wave velocity, which in turn leads to a reduction of the fundamental frequency. As a result, applying equation (1) to estimate the sediment thickness at the site tends to result in an overestimation. Conversely, if the sediment is dense, the thickness will be underestimated. In this study, the parameters a and b in equation (2) were derived from borehole data collected from the central part of the study area. Estimation errors may occur due to different geological conditions when applying this equation to other areas. It should be noted that the use of the Ibs-von Seht relationship for estimating depth of sedimentary layers is based on the assumption that the layers are flat lying without strong velocity gradients (Motazedian *et al.*, 2011). When subsurface

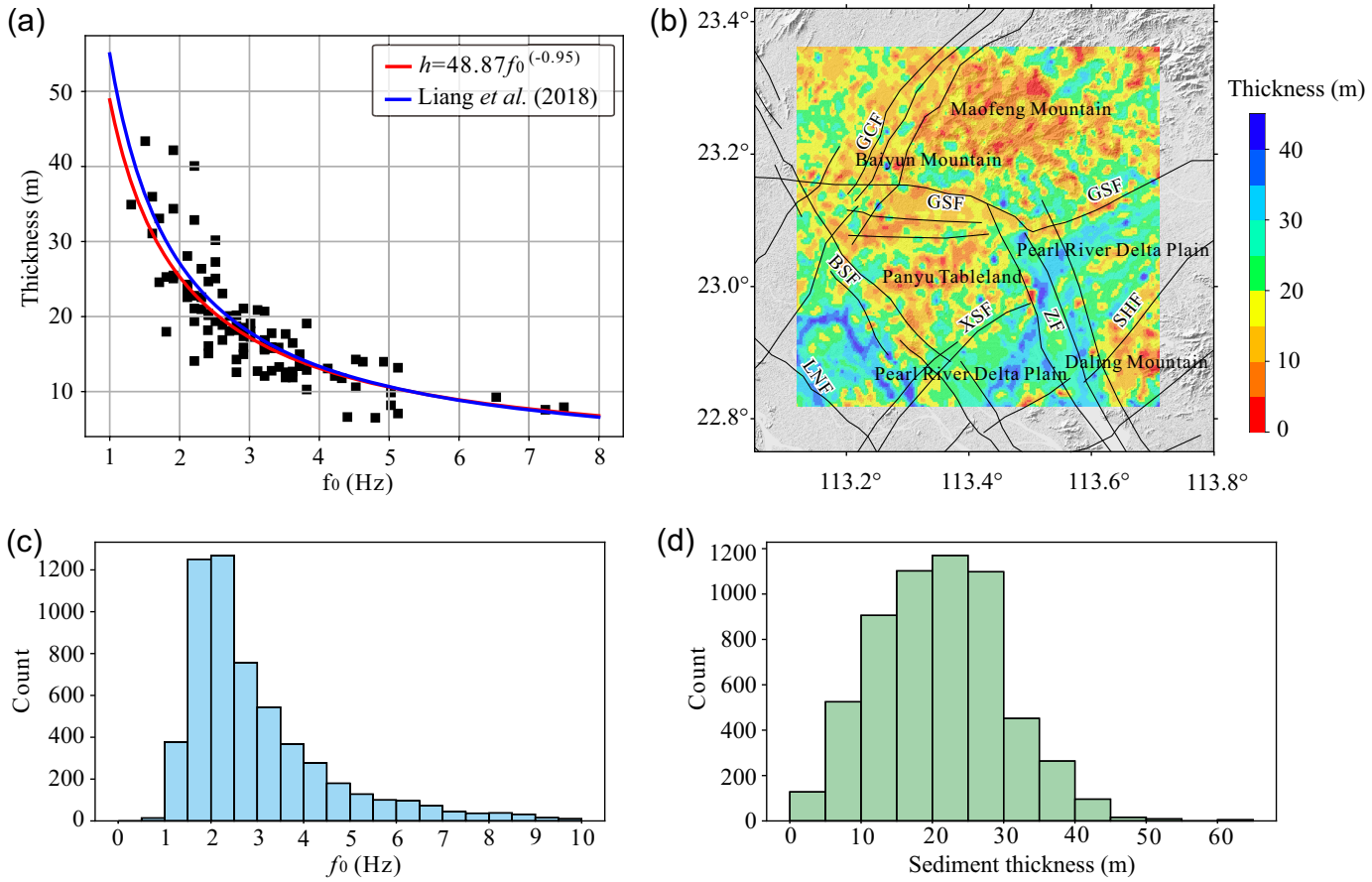

Figure 6. (a) Fundamental frequencies versus the sediment thickness measured at the borehole sites. The red solid line is a fit of equation (1) to the data. The blue solid line is the fit of equation (1) established in Pearl River Delta (PRD) Plain by Liang *et al.* (2018). (b) Distribution of Quaternary sediment thickness across the study area. The black solid lines mark the faults. (c) Histogram of f_0-values. (d) Histogram of Quaternary sediment thickness. The color version of this figure is available only in the electronic edition.

sedimentary layers or topography exhibit significant lateral heterogeneity, this can also affect the accuracy of depth estimates (Guéguen *et al.*, 2007).

Figure 7a displays the Quaternary sediment thickness map compiled based on our collected 3576 geological boreholes, using a 750 m × 750 m equal interval interpolation. Comparatively, the sediment thickness obtained from HVSR, also utilizing a 750 m × 750 m equal interval interpolation (Fig. 7b), is generally consistent with the borehole results. It can be observed that there are some discrepancies in the sediment thickness estimated using boreholes and HVSR (Fig. 7c). Most of the errors are within 5 m (Fig. 7d), with a mean absolute error of 3.25 m and a standard deviation of absolute errors of 2.95 m. This discrepancy can be attributed to different near-surface geological conditions. Nevertheless, this disparity is acceptable for rapid municipal planning and engineer exploration purposes. Overall, the Quaternary sediment thickness acquired using the HVSR method with a 750 m spacing array is comparable to that obtained using dense borehole data. This study demonstrates that employing the HVSR method and dense seismic arrays for microtremor detection, supported by borehole information to establish the f_0–Z relationship, is an effective, efficient, environmentally friendly, and low-cost passive source method suitable for detecting shallow structures in highly populated cities where large-scale drilling and active source investigations are challenging.

Identification and characteristics of the paleochannels

A series of high-thickness anomalies were identified in the southern part of the study area, exhibiting a spatial distribution in stripes. These anomalies displayed an average thickness of Quaternary sediments exceeding 30 m (Fig. 8). The characteristics of these high-thickness anomaly zones, including their width, location, and Quaternary sediment thickness, bear a striking resemblance to the features of the late Pleistocene paleochannels previously documented in the PRD region (Zhuang *et al.*, 2015). For example, the high-thickness anomaly zone between Panyu Tableland and Shiziyang Waterway closely aligns with the location of the paleochannel identified by Zhuang *et al.* (2015) (Fig. 8a). Based on these observations, we posited that these high-thickness anomaly zones correspond to buried paleochannels.

These paleochannels have widths ranging from 2 to 6 km, multiple branching channels, and flow in three primary

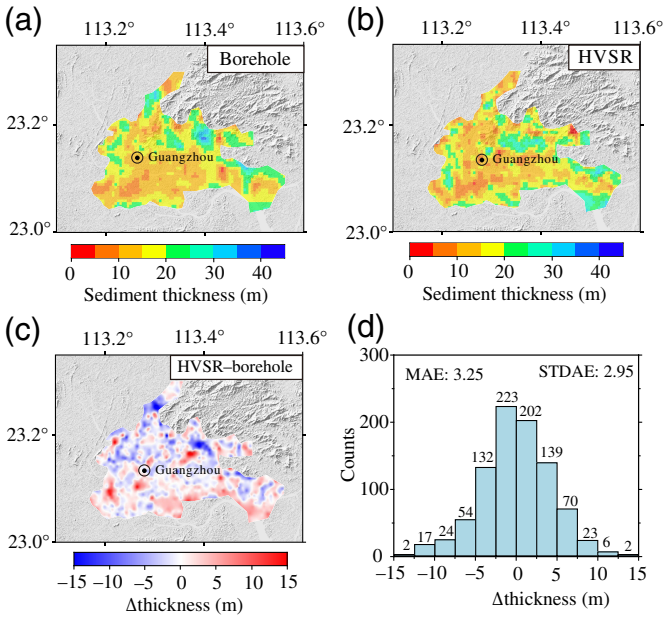

Figure 7. Comparison of Quaternary sediment thickness obtained by two methods in the central part of the research area. The plot range is shown in Figure 1b. (a) Quaternary sediment thickness obtained from dense geological boreholes. (b) Quaternary sediment thickness derived from the HVSR method in this study. (c) Thickness difference between panels (b) and (a). (d) Histogram of the differences between HVSR measurements and borehole measurements. The mean absolute error (MAE) is 3.25 m, and the standard deviation of absolute errors (STDAE) is 2.95 m. The color version of this figure is available only in the electronic edition.

directions: northeast–southwest, northwest–southeast, and near north–south. The majority of paleochannels have thicknesses exceeding 30 m.

To better understand the loose sedimentary structures in the study area, four vertical sections of Quaternary sediment thickness are shown in Figure 8b–e, with south–north sections to the left and west–east sections to the right. Stations within a proximity of 0.5 km on both sides are projected onto the corresponding sections. The vertical sections reveal significant lateral variations in the thickness of Quaternary sediments across the study area. Within these profiles, paleochannels can be readily identified, often cutting into the underlying strata in a "V" or "U" shape. The paleochannels exhibit varying burial depths and scales, ranging from 20 to 40 m, and downcutting depths of 5–20 m. Despite the passage of time, a few paleochannels have persisted to the present day due to topographical and structural constraints. An example of such a persevering river inheritance is observed at the Shiziyang Waterway (45 km distance at D1–D2 profile).

Previous studies have suggested that variable HVSRs obtained from different rotational angles of two horizontal components may indicate complex and spatially variable subsurface structures (Matsushima *et al.*, 2014, 2017; Vantassel *et al.*, 2018; Cheng *et al.*, 2020). Therefore, the azimuthal sensitivity of HVSR measurements is a crucial aspect of understanding the spatial variability of subsurface conditions and may help assess potential 2D and 3D site effects. In this study, we computed the azimuthal variations of HVSR measurements along the C1–C2 profile, following the procedures proposed by Cheng *et al.* (2020) with an interval of 10°. As illustrated in Figure 9a, we compared the f_0 at each measurement point between the north–south ([NS] [0°]) and east–west ([EW] [90°]) orientations against the average azimuth. The results indicate that most measurement points exhibited minimal azimuthal variation in f_0. However, we observed some azimuthal effects at locations near the edges of paleochannels, where rapid changes in sediment layer thickness occur, as well as in areas with topographic variations (~55 km distance). Figure 9b–d represents three types of stations. Figure 9b shows minimal azimuthal variability in both f_0 and amplitude (A_0), and this type of station constitutes a small portion of the total. Figure 9c exhibits limited azimuthal variability in f_0 but displays variability in amplitude, which is the most common characteristic among the analyzed stations. Figure 9d demonstrates both f_0 and amplitude azimuthal variability, though changes in f_0 are not substantial, typically found in areas inferred to be near the edges of paleochannels or on slopes. These observations suggest that azimuthal effects have a minimal impact on the identification of f_0, but they can serve as indicators of subsurface complexity.

Hazard analysis and risk assessment in the GBA

Urban areas are crucial research areas in earthquake disaster studies due to their high population density and economic significance. Over the past century, several strong earthquakes with magnitudes of 6 or greater have occurred in the adjacent areas of the GBA, including the 1969 M_s 6.4 Yangjiang earthquake and the 1962 M_s 6.1 Xinfengjiang earthquake, which vigorously shook the GBA. Recent earthquakes above M_L 4.0 in the offshore GBA, such as the 2020 M_L 4.0 earthquake in offshore Zhuhai and the 2022 M_L 4.6 earthquake in offshore Huidong, have further highlighted the high risk of seismic damage in Guangzhou. In addition, at least 50 locations in Guangzhou have experienced ground subsidence hazards, particularly in the southern part where loose Quaternary sediments are widely distributed. These events have prompted an assessment of the potential seismic and geologic risk in this region.

We analyzed the ground-motion intensity caused by the earthquakes. Figure 10 illustrates the relationship between the horizontal *S*-wave FAS and sediment thickness. We can observe a clear positive correlation between the average amplitude and sediment thickness (Fig. 10b). In Figure 10c, no significant trend is observed between the average amplitude and epicentral distance. However, there is a clear distinction between sites in paleochannels and sites with flat HVSR curves. We categorized the sites into four groups based on sediment

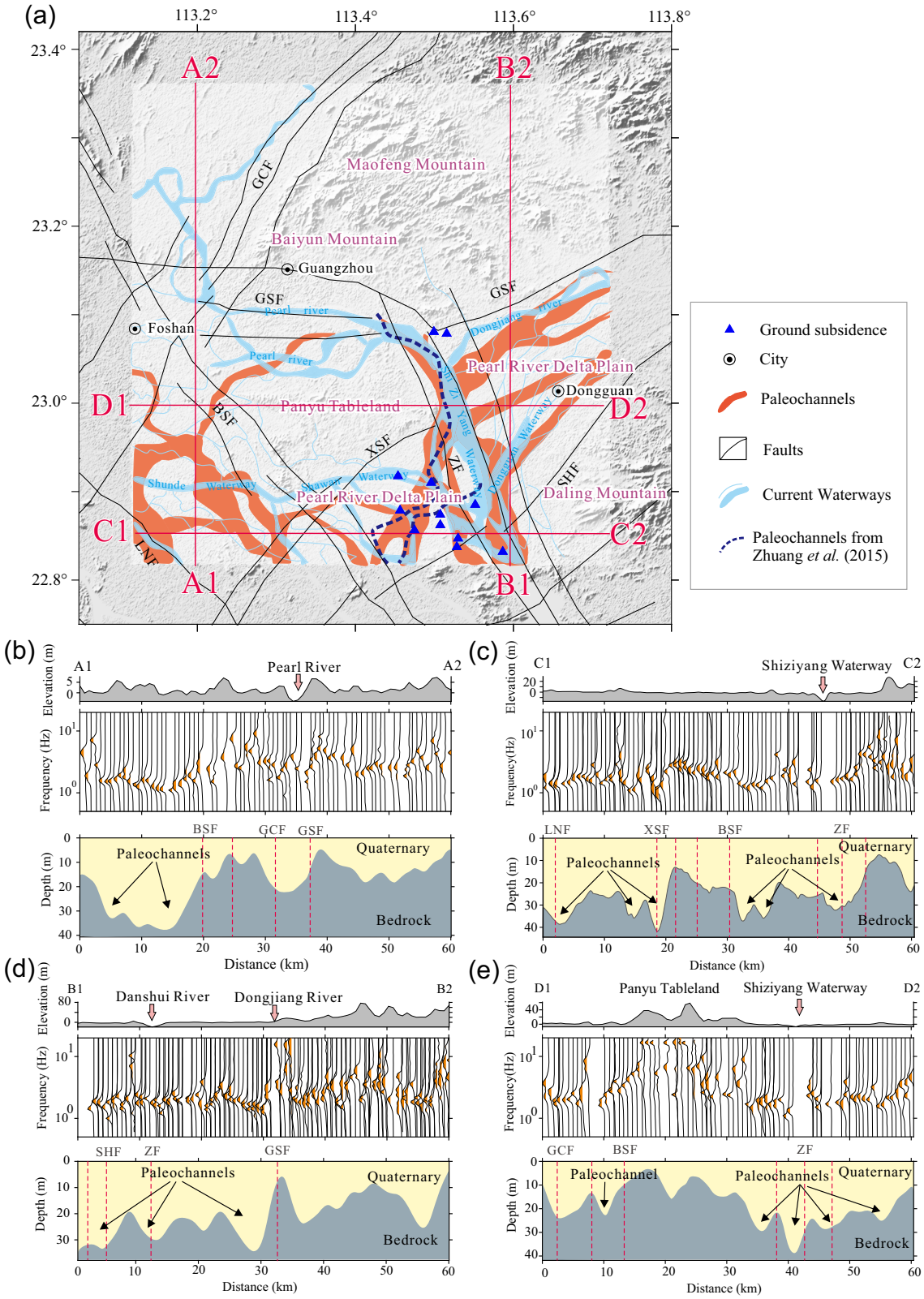

thickness and compared the averaged spectral ratios for each group. Figure 10c,d shows the averaged spectral ratio results obtained from *S* waves of a local earthquake and five regional and teleseismic events, respectively, which yielded similar results. Sites with greater sediment thickness exhibit larger amplitudes and cover a broader frequency range with

Figure 8. (a) The identified spatial distribution of paleochannels. Cross sections illustrating (b) A1–A2, (c) C1–C2, (d) B1–B2, and (e) D1–D2. The upper panel of each section presents the elevation, the middle panel displays the calculated HVSR curves, and the lower panel shows the converted Quaternary sediment thickness. Faults are delineated by purple dashed lines. Paleochannels are outlined with arrows. The color version of this figure is available only in the electronic edition.

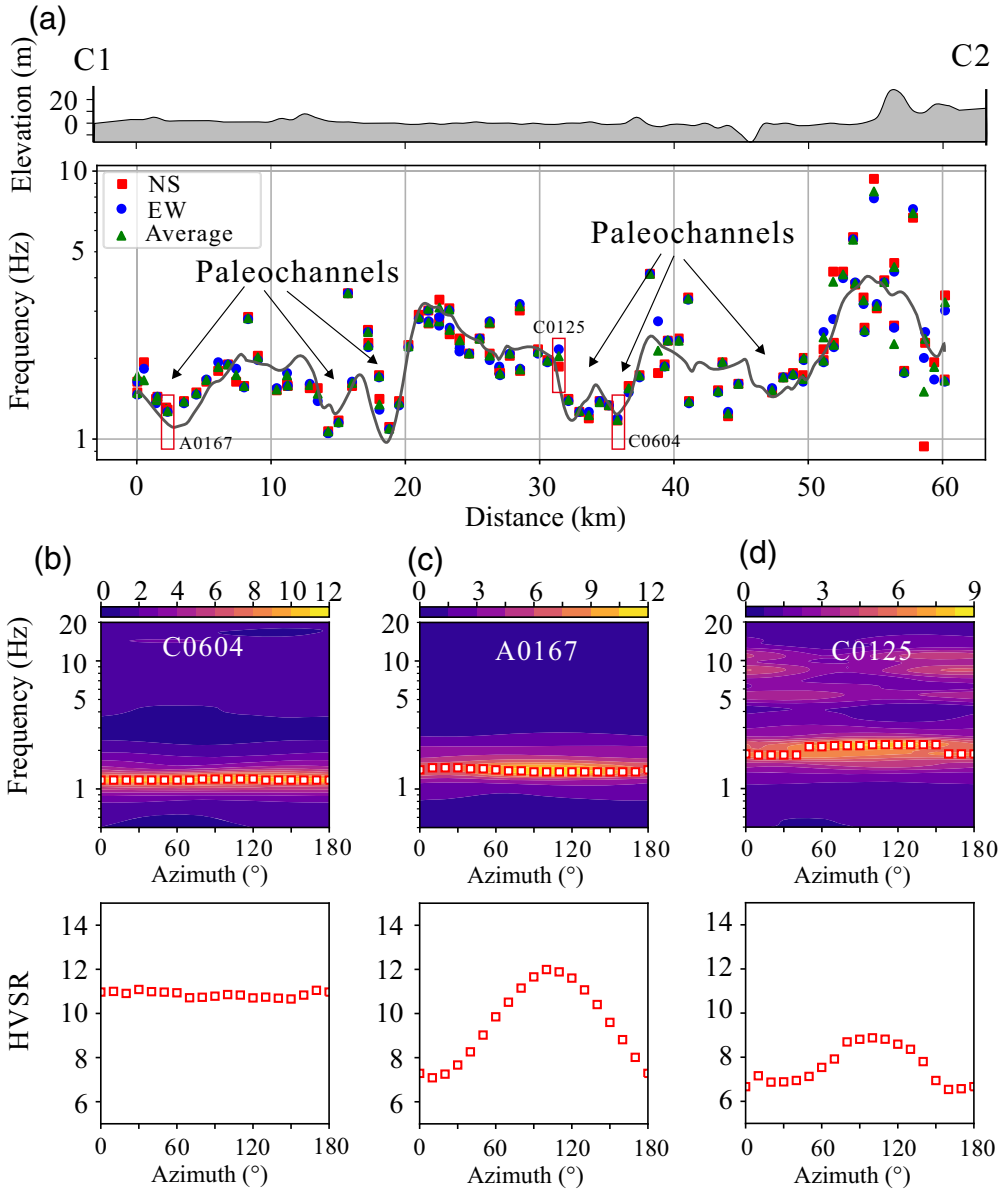

Figure 9. Comparison of HVSR measurements along C1–C2 profile (location shown in Fig. 8a). (a) A comparison of f_0 and azimuthal variability for stations along section C1–C2. The upper panel presents the elevation. (b) Example HVSR data in which f_0 and A_0 show almost no changes with azimuth. (c) Example HVSR data shows limited azimuthal variability in f_0 while displaying variability in amplitude. (d) Example HVSR data demonstrating azimuthal variability in both f_0 and amplitude. The color version of this figure is available only in the electronic edition.

significant amplitudes. Comparatively, the amplitude values for sites with sediment thickness exceeding 30 m can reach as high as 15–25.

In the study area, the paleochannel regions are characterized by the thickest Quaternary sediment deposits, which contribute to lower fundamental frequencies. It can be inferred that the paleochannel regions are more susceptible to experiencing maximum ground motion during strong earthquakes (Fig. 10). Previous studies have also reported that paleochannel areas are more vulnerable to significant damage during solid earthquakes in other regions. For instance, during the 1966 Xingtai M_s 7.2 earthquake in China, over 90% of the houses located on the paleochannels suffered severe damage and collapse, whereas only 30% of the houses situated hundreds of meters away from the paleochannels were similarly affected (Sun, 1985). A similar phenomenon was observed during the 2001 M_w 7.7 Bhuj earthquake, where the city of Ahmedabad in western India experienced significant damage due to the effect of paleochannels despite being 250 km away from the epicenter (Sairam *et al.*, 2018).

From the geological perspective, paleochannels represent distinct geological formations composed of loosely packed, weakly compressive, and water-rich sandstone. Horizontally, the sediments within and outside the paleochannels exhibit substantial differences in terms of particle size, sorting, density, degree of consolidation, compressive strength, shear force, and other physical and mechanical properties (Zhang *et al.*, 2016). Abrupt variations in mechanical support within a limited spatial span can lead to substantial risk to large-scale engineering projects. Furthermore, the lateral variations in the geological structure can lead to 2D and 3D site effects during seismic events (Thompson *et al.*, 2012; Pilz and Cotton, 2019). Vertically, the paleochannels are in nonconformable contact with the underlying rock, and the material properties of sediments deposited during different geological periods vary significantly. The uneven settlement characteristics of these sediments can result in uneven stress distribution on building foundations, leading to tilting. In Guangzhou city, it has been observed that the locations of ground subsidence hazards are primarily concentrated in the paleochannel areas (Fig. 8a). Therefore, special attention should be given to these paleochannel areas when assessing and managing the risks associated with Quaternary soft sediments.

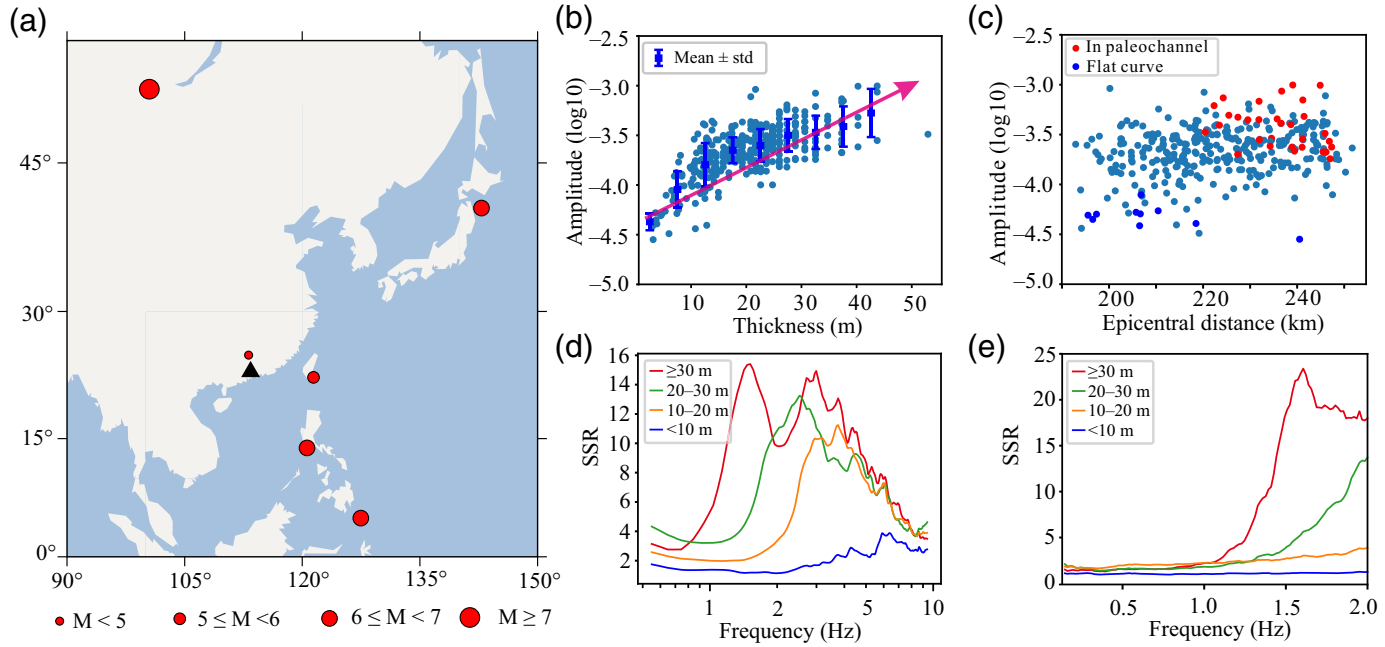

Figure 10. Relationship between *S*-wave frequency amplitude spectrum and sediment thickness. (a) Locations of earthquakes used in the ground-motion analyses. The black triangle shows the location of the seismic array. (b) Distribution of average amplitude (in log10 unit) of 0.5–10 Hz from *S* waves of a local earthquake versus sediment thickness. (c) Distribution of average amplitude (in log10 unit) of 0.5–10 Hz from *S* waves of a local earthquake versus epicentral distance. (d) The averaged spectral ratio results obtained from *S* waves of a local earthquake for different sediment thickness categories. (e) The averaged spectral ratio results were obtained from *S* waves of five regional and teleseismic events for different sediment thickness categories. The color version of this figure is available only in the electronic edition.

CONCLUSIONS

This study employed a dense array and the HVSR method to investigate the Quaternary sediment thicknesses and their associated site effects on the GBA. In general, our findings agree well with the surface geology. Specifically, we observed that the Quaternary sedimentary layer in mountainous areas has an average thickness of less than 10 m, fundamental frequencies exceeding 4.5 Hz. In contrast, the Quaternary sedimentary layer within the PRD Plain is notably thicker, with thickness exceeding 20 m and fundamental frequencies below 3 Hz. Furthermore, we successfully identified and delineated the spatial distribution and geometric properties of the late Pleistocene paleochannels within the study area. Notably, these paleochannel areas pose potential seismic and geologic hazards, making them worthy of more attention. This study provides valuable insights into the near-surface loose sediment layers, shedding light on urban construction and disaster risk assessment.

DATA AND RESOURCES

The obtained fundamental frequency, peak amplitude, and sediment thickness are provided by Deng (2024). The microtremor recording data that support the findings of this study are included and will be available from the corresponding author(s) upon reasonable request. The supplemental material includes detailed event information analyzed in this study.

DECLARATION OF COMPETING INTERESTS

The authors acknowledge that there are no conflicts of interest recorded.

ACKNOWLEDGMENTS

The authors gratefully acknowledge Xiaoming Lin for his valuable comments. The authors thank the Guangdong Provincial Geological Survey Institute for providing the fault distribution. The authors appreciate the helpful discussions with colleagues at the Group Geophysics_lab, GIGCAS. The authors also thank Editor-in-Chief P. Martin Mai, Associate Editor Céline Beauval, and the two anonymous reviewers for their constructive comments that helped us improve the original article. This work is supported by the National Nature Science Foundation of China (U1901602, 42322401), the National Key Research and Development Program of China (2023YFC3008602).

REFERENCES

Agostini, L., J. Boaga, A. Galgaro, and A. Ninfo (2015). HVSR technique in near-surface thermal-basin characterization: The example of the Caldiero district (North-East Italy), *Environ. Earth Sci.* **74,** no. 2, 1199–1210, doi: 10.1007/s12665-015-4109-0.

Bao, F., Z. Li, D. A. Yuen, J. Zhao, J. Ren, B. Tian, and Q. Meng (2018). Shallow structure of the Tangshan fault zone unveiled by dense seismic array and horizontal-to-vertical spectral ratio method, *Phys. Earth Planet. Int.* **281,** nos. 46/54, doi: 10.1016/j.pepi.2018.05.004.

Beroya, M. A. A., A. Aydin, R. Tiglao, and M. Lasala (2009). Use of microtremor in liquefaction hazard mapping, *Eng. Geol.* **107,** no. 3, 140–153, doi: 10.1016/j.enggeo.2009.05.009.

Borcherdt, R. D. (1970). Effects of local geology on ground motion near San Francisco Bay, *Bull. Seismol. Soc. Am.* **60,** no. 1, 29–61.

Chatelain, J.-L., B. Guillier, F. Cara, A.-M. Duval, K. Atakan, P.-Y. Bard, and , and Wp02 Sesame Team (2008). Evaluation of the influence of experimental conditions on H/V results from ambient noise recordings, *Bull. Earthq. Eng.* **6,** no. 1, 33–74, doi: 10.1007/s10518-007-9040-7.

Chen, Q., L. Liu, W. Wang, and E. Rohrbach (2009). Site effects on earthquake ground motion based on microtremor measurements for metropolitan Beijing, *Chin. Sci. Bull.* **54,** no. 2, 280–287, doi: 10.1007/s11434-008-0422-2.

Cheng, T., B. R. Cox, J. P. Vantassel, and L. Manuel (2020). A statistical approach to account for azimuthal variability in single-station HVSR measurements, *Geophys. J. Int.* **223**, no. 2, 1040–1053, doi: 10.1093/gji/ggaa342.

Cox, B. R., T. Cheng, J. P. Vantassel, and L. Manuel (2020). A statistical representation and frequency-domain window-rejection algorithm for single-station HVSR measurements, *Geophys. J. Int.* **221,** no. 3, 2170–2183, doi: 10.1093/gji/ggaa119.

Dal Moro, G., and G. F. Panza (2022). Multiple-peak HVSR curves: Management and statistical assessment, *Eng. Geol.* **297,** 106500, doi: 10.1016/j.enggeo.2021.106500.

Deng, Y. (2024). Data for the Greater Bay Area, South China, figshare, Dataset, doi: 10.6084/m9.figshare.26190869.v1.

Dong, S., L. Li, L. Zhao, X. Shen, W. Wang, H. Huang, B. Peng, X. Xu, and R. Gao (2022). Seismic evidence for fluid-driven pore pressure increase and its links with induced seismicity in the Xinfengjiang Reservoir, South China, *J. Geophys. Res.* **127,** no. 3, e2021JB023548, doi: 10.1029/2021JB023548.

Farazi, A. H., Y. Ito, E. S. M. Garcia, A. M. Lontsi, F. J. Sánchez-Sesma, A. Jaramillo, S. Ohyanagi, R. Hino, and M. Shinohara (2023). Shear wave velocity structure at the Fukushima forearc region based on H/V analysis of ambient noise recordings by ocean bottom seismometers, *Geophys. J. Int.* **233,** no. 3, 1801–1820, doi: 10.1093/gji/ggad028.

Gallipoli, M. R., G. Calamita, N. Tragni, D. Pisapia, M. Lupo, M. Mucciarelli, T. A. Stabile, A. Perrone, L. Amato, F. Izzi, *et al.* (2020). Evaluation of soil-building resonance effect in the urban area of the city of Matera (Italy), *Eng. Geol.* **272,** 105645, doi: 10.1016/j.enggeo.2020.105645.

Guéguen, P., J.-L. Chatelain, B. Guillier, H. Yepes, and J. Egred (1998). Site effect and damage distribution in Pujili (Ecuador) after the 28 March 1996 earthquake, *Soil Dynam. Earthq. Eng.* **17,** no. 5, 329–334, doi: 10.1016/S0267-7261(98)00019-0.

Guéguen, P., C. Cornou, S. Garambois, and J. Banton (2007). On the limitation of the H/V spectral ratio using seismic noise as an exploration tool: Application to the Grenoble Valley (France), a Small Apex Ratio Basin, *Pure Appl. Geophys.* **164,** 115–134, doi: 10.1007/s00024-006-0151-x.

Ibs-von Seht, M., and J. Wohlenberg (1999). Microtremor measurements used to map thickness of soft sediments, *Bull. Seismol. Soc. Am.* **89,** no. 1, 250–259, doi: 10.1785/bssa0890010250.

Kanai, K., and T. Tanaka (1961). On microtremor VIII, *Bull. Earthq. Res. Inst.* **39,** 97–114.

Konno, K., and T. Ohmachi (1998). Ground-motion characteristics estimated from spectral ratio between horizontal and vertical components of microtremor, *Bull. Seismol. Soc. Am.* **88,** no. 1, 228–241, doi: 10.1785/bssa0880010228.

Lachet, C. D., and P.-Y. Bard (1994). Numerical and Theoretical Investigations on the Possibilities and Limitations of Nakamura's Technique, *J. Phys. Earth* **42,** no. 5, 377–397, doi: 10.4294/jpe1952.42.377.

Liang, D., F. Gan, W. Zhang, and L. Jia (2018). The application of HVSR method in detecting sediment thickness in karst collapse area of Pearl River Delta, China, *Environ. Earth Sci.* **77,** no. 6, 259, doi: 10.1007/s12665-018-7439-x.

Lin, F.-C., D. Li, R. W. Clayton, and D. Hollis (2013). High-resolution 3D shallow crustal structure in Long Beach, California: Application of ambient noise tomography on a dense seismic array, *Geophysics* **78,** no. 4, Q45–Q56, doi: 10.1190/geo2012-0453.1.

Lunedei, E., and D. Albarello (2010). Theoretical HVSR curves from full wavefield modelling of ambient vibrations in a weakly dissipative layered Earth, *Geophys. J. Int.* **181,** no. 2, 1093–1108, doi: 10.1111/j.1365-246X.2010.04560.x.

Maklad, M., T. Yokoi, T. Hayashida, M. N. ElGabry, H. M. Hassan, H. M. Hussein, T. A. Fattah, and M. Rashed (2020). Site characterization in Ismailia, Egypt using seismic ambient vibration array, *Eng. Geol.* **279,** 105874, doi: 10.1016/j.enggeo.2020.105874.

Matsushima, S., T. Hirokawa, F. De Martin, H. Kawase, and F. J. Sánchez-Sesma (2014). The effect of lateral heterogeneity on horizontal-to-vertical spectral ratio of microtremors inferred from observation and synthetics, *Bull. Seismol. Soc. Am.* **104**, no. 1, 381–393, doi: 10.1785/0120120321.

Matsushima, S., H. Kosaka, and H. Kawase (2017). Directionally dependent horizontal-to-vertical spectral ratios of microtremors at Onahama, Fukushima, Japan, *Earth Planets Space* **69**, no. 1, 96, doi: 10.1186/s40623-017-0680-9.

Molnar, S., A. Sirohey, J. Assaf, P. Y. Bard, S. Castellaro, C. Cornou, B. Cox, B. Guillier, B. Hassani, H. Kawase, *et al.* (2022). A review of the microtremor horizontal-to-vertical spectral ratio (MHVSR) method, *J. Seismol.* **26,** no. 4, 653–685, doi: 10.1007/s10950-021-10062-9.

Motazedian, D., K. Khaheshi Banab, J. A. Hunter, S. Sivathayalan, H. Crow, and G. Brooks (2011). Comparison of site periods derived from different evaluation methods, *Bull. Seismol. Soc. Am.* **101,** no. 6, 2942–2954, doi: 10.1785/0120100344.

Nakamura, Y. (1989). A method for dynamic characteristics estimation of subsurface using microtremor on the ground surface, *Q. Rep. Railway Tech. Res. Inst.* **30,** no. 1, 25–33.

Nogoshi, M., and T. Igarashi (1971). On the amplitude characteristics of microtremor (Part 2), *J. Seismol. Soc. Jpn.* **24,** 26–40.

Olsen, K. B. (2000). Site amplification in the Los Angeles Basin from three-dimensional modeling of ground motion, *Bull. Seismol. Soc. Am.* **90,** no. 6B, S77–S94, doi: 10.1785/0120000506.

Panou, A. A., N. Theodulidis, P. Hatzidimitriou, K. Stylianidis, and C. B. Papazachos (2005). Ambient noise horizontal-to-vertical spectral ratio in site effects estimation and correlation with seismic damage distribution in urban environment: The case of the city of Thessaloniki (Northern Greece), *Soil Dynam. Earthq. Eng.* **25,** no. 4, 261–274, doi: 10.1016/j.soildyn.2005.02.004.

Peng, Y., Z. Wang, E. W. Woolery, Y. Lyu, N. S. Carpenter, Y. Fang, and S. Huang (2020). Ground-motion site effect in the Beijing metropolitan area, *Eng. Geol.* **266,** 105395, doi: 10.1016/j.enggeo.2019.105395.

Perron, V., C. Gélis, B. Froment, F. Hollender, P.-Y. Bard, G. Cultrera, and E. M. Cushing (2018). Can broad-band earthquake site responses be predicted by the ambient noise spectral ratio? Insight from observations at two sedimentary basins, *Geophys. J. Int.* **215,** no. 2, 1442–1454, doi: 10.1093/gji/ggy355.

Picotti, S., R. Francese, M. Giorgi, F. Pettenati, and J. M. Carcione (2017). Estimation of glacier thicknesses and basal properties using the horizontal-to-vertical component spectral ratio (HVSR) technique from passive seismic data, *J. Glaciol.* **63,** no. 238, 229–248, doi: 10.1017/jog.2016.135.

Picotti, S., S. Parolai, and D. Albarello (2005). Statistical analysis of noise horizontal-to-vertical spectral ratios (HVSR), *Bull. Seismol. Soc. Am.* **95,** no. 5, 1779–1786, doi: 10.1785/0120040152.

Pilz, M., and F. Cotton (2019). Does the one-dimensional assumption hold for site response analysis? A study of seismic site responses and implication for ground motion assessment using KiK-Net strong-motion data, *Earthq. Spectra* **35,** no. 2, 883–905, doi: 10.1193/050718EQS113M.

Pontrelli, M., L. Baise, and J. Ebel (2023). Regional-scale site characterization mapping in high impedance environments using soil fundamental resonance (f0): New England, USA, *Eng. Geol.* **315,** 107043, doi: 10.1016/j.enggeo.2023.107043.

Pratt, T. L., and L. S. Schleicher (2021). Characterizing ground-motion amplification by extensive flat-lying sediments: The seismic response of the Eastern U.S. Atlantic Coastal Plain Strata, *Bull. Seismol. Soc. Am.* **111,** no. 4, 1795–1823, doi: 10.1785/0120200328.

Sairam, B., A. P. Singh, V. Patel, V. Pancholi, S. Chopra, V. K. Dwivedi, and M. Ravi Kumar (2018). Influence of local site effects in the Ahmedabad mega city on the damage due to past earthquakes in Northwestern India, *Bull. Seismol. Soc. Am.* **108,** no. 4, 2170–2182, doi: 10.1785/0120170266.

Seed, H. B., M. P. Romo, J. I. Sun, A. Jaime, and J. Lysmer (1988). The Mexico earthquake of September 19, 1985—relationships between soil conditions and earthquake ground motions, *Earthq. Spectra* **4,** no. 4, 687–729, doi: 10.1193/1.1585498.

Site EffectS Assessment Using Ambient Excitations (SESAME) (2004). Guidelines for the implementation of the H/V spectral ratio technique on ambient vibrations measurements, processing and interpretation, http://sesame.geopsy.org/Papers/HV_User_Guidelines.pdf (last accessed November 2024).

Sivaram, K., P. Mahesh, and S. S. Rai (2012). Stability assessment and quantitative evaluation of H/V spectral ratios for site response studies in Kumaon Himalaya, India using ambient noise recorded by a broadband seismograph network, *Pure Appl. Geophys.* **169,** no. 10, 1801–1820, doi: 10.1007/s00024-011-0436-6.

Song, J., and H. Yang (2022). Seismic site response inferred from records at a dense linear array across the Chenghai Fault Zone, Binchuan, Yunnan, *J. Geophys. Res.* **127,** no. 1, e2021JB022710, doi: 10.1029/2021JB022710.

Sun, Z. (1985). Paleochannels–disappeared rivers, *Earth* **3,** 28–29.

Thompson, E. M., L. G. Baise, Y. Tanaka, and R. E. Kayen (2012). A taxonomy of site response complexity, *Soil Dynam. Earthq. Eng.* **41,** 32–43, doi: 10.1016/j.soildyn.2012.04.005.

Vantassel, J., (2021). jpvantassel/hvsrpy: v1.0.0, *Zenodo*, doi: 10.5281/zenodo.5563211.

Vantassel, J., B. Cox, L. Wotherspoon, and A. Stolte (2018). Mapping depth to bedrock, shear stiffness, and fundamental site period at CentrePort, Wellington, using surface-wave methods: Implications for local seismic site amplification, *Bull. Seismol. Soc. Am.* **108,** no. 3B, 1709–1721, doi: 10.1785/0120170287.

Wathelet, M., J. L. Chatelain, C. Cornou, G. D. Giulio, B. Guillier, M. Ohrnberger, and A. Savvaidis (2020). Geopsy: A user-friendly open-source tool set for ambient vibration processing, *Seismol. Res. Lett.* **91,** no. 3, 1878–1889, doi: 10.1785/0220190360.

Woolery, E. W., and R. Street (2002). 3D near-surface soil response from H/V ambient-noise ratios, *Soil Dynam. Earthq. Eng.* **22,** no. 9, 865–876, doi: 10.1016/S0267-7261(02)00109-4.

Xiong, C., X. Ye, Z. Guo, L. Wang, X. Wu, Y. Zhang, and Z. Lv (2024). High-resolution 3D shallow s-wave velocity structure revealed by ambient-noise double beamforming with a dense array in Guangzhou Urban Area, China, *Seismol. Res. Lett.* **95,** no. 6, 3665–3680, doi: 10.1785/0220230405.

Yan, P., Z. Li, F. Li, Y. Yang, W. Hao, and F. Bao (2018). Antarctic ice sheet thickness estimation using the horizontal-to-vertical spectral ratio method with single-station seismic ambient noise, *Cryosphere* **12,** no. 2, 795–810, doi: 10.5194/tc-12-795-2018.

Yang, S., G. P. Mavroeidis, J. C. de la Llera, A. Poulos, P. Aguirre, S. Rahpeyma, T. Sonnemann, and B. Halldorsson (2019). Empirical site classification of seismological stations in Chile using horizontal-to-vertical spectral ratios determined from recordings of large subduction-zone earthquakes, *Soil Dynam. Earthq. Eng.* **125,** 105678, doi: 10.1016/j.soildyn.2019.05.017.

Ye, X., L. Wang, C. Xiong, X. Wang, G. Wen, D. Yu, Z. Guo, W. Wang, Z. Lv, H. Wu, *et al.* (2024). Shallow 3D structure investigation of some cities in the Guangdong–Hong Kong–Macao Greater Bay Area, *Seismol. Res. Lett.* **95,** no. 3, 2000–2012, doi: 10.1785/0220230155.

Zeckra, M., K. Van Noten, and T. Lecocq (2022). Sensitivity, accuracy and limits of the lightweight three-component SmartSolo geophone sensor (5 Hz) for seismological applications, doi: 10.31223/X5F073.

Zhang, Z., Z. Wei, H. He, W. Wei, L. Qian, and T. Li (2016). Potential submarine geologic hazards at the entrance of the Pearl River Estuary in the northern South China Sea, *J. Ocean Univ. China* **15,** no. 4, 606–612, doi: 10.1007/s11802-016-2868-1.

Zhou, G., and H. Yao (2024). Shallow structure and seismic amplification effects in the Weifang Segment of the Tanlu fault zone based on the spectral ratio method, *Seismol. Res. Lett.* doi: 10.1785/0220240150.

Zhou, Q., and X. Shen (2021). Comparison and analysis of the observations from broadband and short-period seismometers in noisy environment, *Progr. Geophys.* **36,** no. 5, 1916–1926.

Zhuang, W., Y. Huang, and X. Lin (2015). *Urban Geology of Guangzhou*, Geological Publishing House, Beijing.

Manuscript received 27 August 2024